ADVANCES IN ATMOSPHERIC SCIENCES, VOL. 39, JULY 2022, 1115–1132

• **Original Paper** •

Improving Simulations of Vegetation Dynamics over the Tibetan Plateau: Role of Atmospheric Forcing Data and Spatial Resolution※

Zhijie KANG[1], Bo QIU[*1], Zheng XIANG[1], Ye LIU[2], Zhiqiang LIN[3], and Weidong GUO[*1]

[1]*School of Atmospheric Sciences*, *Nanjing University*, *Nanjing* 210046, *China*

[2]*Pacific Northwest National Laboratory*, *Washington* 99354, *USA*

[3]*Plateau Atmosphere and Environment Key Laboratory of Sichuan Province*, *School of Atmospheric Sciences*, *Chengdu University of Information Technology*, *Chengdu* 610225, *China*

(Received 16 November 2021; revised 19 February 2022; accepted 15 March 2022)

ABSTRACT

The efficacy of vegetation dynamics simulations in offline land surface models (LSMs) largely depends on the quality and spatial resolution of meteorological forcing data. In this study, the Princeton Global Meteorological Forcing Data (PMFD) and the high spatial resolution and upscaled China Meteorological Forcing Data (CMFD) were used to drive the Simplified Simple Biosphere model version 4/Top-down Representation of Interactive Foliage and Flora Including Dynamics (SSiB4/TRIFFID) and investigate how meteorological forcing datasets with different spatial resolutions affect simulations over the Tibetan Plateau (TP), a region with complex topography and sparse observations. By comparing the monthly Leaf Area Index (LAI) and Gross Primary Production (GPP) against observations, we found that SSiB4/TRIFFID driven by upscaled CMFD improved the performance in simulating the spatial distributions of LAI and GPP over the TP, reducing RMSEs by 24.3% and 20.5%, respectively. The multi-year averaged GPP decreased from 364.68 gC m^{-2} yr^{-1} to 241.21 gC m^{-2} yr^{-1} with the percentage bias dropping from 50.2% to –1.7%. When using the high spatial resolution CMFD, the RMSEs of the spatial distributions of LAI and GPP simulations were further reduced by 7.5% and 9.5%, respectively. This study highlights the importance of more realistic and high-resolution forcing data in simulating vegetation growth and carbon exchange between the atmosphere and biosphere over the TP.

Key words: SSiB4, meteorological forcing data, vegetation dynamics, spatial resolution, Tibetan Plateau

Citation: Kang, Z. J., B. Qiu, Z. Xiang, Y. Liu, Z. Q. Lin, and W. D. Guo, 2022: Improving simulations of vegetation dynamics over the Tibetan Plateau: Role of atmospheric forcing data and spatial resolution. *Adv. Atmos. Sci.*, **39**(7), 1115–1132, https://doi.org/10.1007/s00376-022-1426-6.

Article Highlights:

- Vegetation dynamics over the Tibetan Plateau (TP) were simulated and analyzed with a dynamic vegetation model.
- Atmospheric forcing data significantly affected the simulations of Leaf Area Index (LAI) and Gross Primary Production (GPP) over the TP.
- China Meteorological Forcing Data (CMFD) largely improved vegetation growth and carbon exchange simulations over the TP.

1. Introduction

Vegetation growth strongly influences the surface radiation balance, water, energy, and carbon cycles, and climate change on regional and global scales. Different vegetation types affect the absorption of solar shortwave radiation and emission of longwave radiation owing to altered surface albedos, which have a profound impact on regional and global surface energy budgets (Giambelluca et al., 1997). The standing vegetation controls the drag coefficient, roughness length, and displacement height, altering the exchange of momentum and heat flux (Dong et al., 2001). In addition, vegetation transports water and latent and sensible heat from the soil into the atmosphere through stomata (Goudriaan and Waggoner, 1972; Chen, 1984). Meanwhile, CO_2 is

※ This paper is a contribution to the special issue on Third Pole Atmospheric Physics, Chemistry, and Hydrology.

* Corresponding authors: Bo QIU, Weidong GUO
Emails: qiubo@nju.edu.cn, guowd@nju.edu.cn

assimilated from the atmosphere to plants through photosynthesis, offsetting large amounts of anthropogenic carbon emissions (Cox and Jones, 2008). Therefore, modern Land Surface Models (LSMs) and Earth System Models (ESMs) must efficiently simulate biogeophysical and biochemical processes to improve climate projections at various spatial and temporal scales.

With an average elevation of more than 4000 m and a total area of more than 2.5 million km^2, the Tibetan Plateau (TP) is known as the world's "third pole". It acts as a weak heat sink in winter and a large heat source in summer, functioning as a giant air pump to force air column descent and ascent, strongly influencing regional atmospheric circulation and having significant impacts on climate change in the Northern Hemisphere (Wu et al., 2007). Known as the "Asian Water Tower", the TP is the source of most of Asia's major rivers and provides water to over 1.4 billion people (Immerzeel et al., 2010). In recent decades, the TP has experienced pronounced warming at a rate that is twice the global average, making it highly vulnerable to climate change. Current studies show that climate change influences vegetation structure and its ecological functioning in the TP. Changes in the length of the growing season and photosynthetic rates significantly impact vegetation uptake (Jeong et al., 2011). Changes in vegetation variability over the TP also provide feedback to the regional climate (Collatz et al., 2000; Shen et al., 2015). For instance, Shen et al. (2015) showed that increasing seasonal vegetation activity over the TP could attenuate surface warming by enhancing evapotranspiration. Currently, most studies suggest that regional warming and precipitation changes play an important role in the variation of vegetation over the TP, and it is widely agreed that warming is the dominant factor for increasing vegetation in the TP (Zhong et al., 2019). The impact of precipitation on vegetation changes presents a complex relationship in different areas and seasons, whereas elevation has a noticeable impact on the effects of warming and precipitation on vegetation change (Liu et al., 2019b). The factors influencing vegetation change are complex and diverse, making LSMs important tools for studying vegetation dynamics in the TP.

Significant progress has recently been made concerning the development of biophysical and biochemical processes in LSMs. Based on the "Big Leaf" model, Sellers et al. (1986) developed the Simple Biosphere Model (SiB) to mimic the flow of energy, water, and momentum in climate between vegetation and the atmosphere. Since the late 1980s, global climate change has become a significant issue. Many scientists have realized that carbon sinks from terrestrial ecosystems play a vital role in climate change; thus, more comprehensive LSMs, which directly couple water and carbon processes, should have been developed. Sellers et al. (1996) incorporated the photosynthesis-stomatal conductance model in SiB2, indicating which LSMs were more realistic for connecting water, energy, and carbon fluxes simultaneously. Efforts have been made to improve simulations through land surface parameter development as the number of coupled parameterization schemes has grown. Lü and Ji (2002a, b) updated parameterization schemes for physiological processes in the Atmosphere-Vegetation Interaction Model (AVIM), such as carbon allocation and vegetation phenology, and proceeded to simulate the spatial distribution of LAI and NPP on the TP. Yu et al. (2011) improved the seasonal variations of vegetation by optimizing the phenological scheme in the dynamic vegetation model. To assess the ability of vegetation transpiration, De Kauwe et al. (2015) used the plant functional type to constrain the the parameter of plant water use strategy. Zhang et al. (2015) tweaked the competition coefficients, the optimal temperature for photosynthesis, and leaf drop threshold temperatures in the SSiB4/TRIFFID, which improved the simulation of the distributions of dominant vegetation types, vegetation fraction, and leaf area index (LAI). Yang et al. (2019) and Dan et al. (2020) introduced nitrogen dynamics into LSMs and improved simulations of carbon uptake in the terrestrial ecosystem. Various methods have been used to further optimize land surface parameters in LSMs (Li et al., 2011; Bastrikov et al., 2018).

Despite improvements, LSMs are inaccurate when simulating biogeophysical and biochemical processes. Simplified parameterization approaches, unrealistic land surface characteristics, and meteorological forcing data impact model performance (Duan et al., 2006). Meteorological forcing data required by LSMs, includes precipitation, air temperature at two meters above the surface, downward shortwave radiation, downward longwave radiation, wind speed, specific humidity, and pressure. Previous studies have suggested that the quality of LSM simulations varies with the quality of the meteorological forcing data. Jung et al. (2007) pointed out that the choice of meteorological forcing data could affect the magnitude and spatiotemporal patterns of gross primary productivity (GPP) simulations. Liu et al. (2019a) demonstrated that an LSM simulation with accurate regional atmospheric forcing data could better simulate regional-scale land surface hydrological processes.

Lacking model resolution and fine-scale observations have been found as a source of cold and wet biases in regional and global climate models of the TP (Su et al., 2013; Meng et al., 2018). LSMs require realistic and high spatial-resolution meteorological data, such as temperature and precipitation, to improve the outcome. The CMFD has been developed as the first high-resolution meteorological dataset (Yang et al., 2010; He et al., 2020). The CMFD accuracy has increased with the fusion of remote sensing products, reanalysis datasets, and in-situ station data. The data has been used to (i) improve simulations such as permafrost and soil moisture in LSMs (Chen et al., 2011; Guo and Wang, 2013), (ii) improve surface parameters (Sun et al., 2016; Chen et al., 2021), and (iii) drive the land assimilation systems (Yang et al., 2020). For example, Chen et al. (2011) compared the simulations of land surface temperature with the Institute of Tibetan Plateau Research, Chinese Academy of Sciences (ITPCAS), and the Global Land Data

Assimilation System (GLADS) forcing data in LSM. They found that the land surface temperature simulation with CMFD cooled by more than 2°C. Guo and Wang (2013) used ITPCAS forcing data to model more detailed permafrost and seasonally frozen ground states. More studies have been conducted for carbon cycle simulations (Sun et al., 2016), hydrological cycle simulations (Long et al., 2018), and energy and water budgets (Lan et al., 2021). A comparison of CMFD with global coarse spatial resolution meteorological forcing data (Princeton Global Meteorological Forcing Data, PMFD) simulations of vegetation dynamics over the TP was made.

In this study, two meteorological forcing datasets were used to investigate the improvement of vegetation dynamics simulations with realistic and high-resolution meteorological forcing data over the TP with the SSiB4/TRIFFID land surface model (Xue et al., 1991; Zhan et al., 2003; Zhang et al., 2015). We chose LAI and GPP to evaluate the simulations because of their importance in water, energy, and carbon exchanges between the atmosphere and the terrestrial ecosystem. Section 2 briefly describes the SSiB4/TRIFFID, meteorological forcing datasets, validation data, evaluation metrics, and experimental design. In section 3, we compared and assessed the three simulations of LAI and GPP against the observations. Discussions and conclusions are presented in sections 4 and 5, respectively.

2. Model, data, evaluation metrics, and experimental design

2.1. *Model description*

The Simplified Simple Biosphere model (SSiB) (Sellers et al., 1986) simulates the exchange of surface energy balance and carbon and water cycles (Xue et al., 1991). The second version of SSiB (SSiB2) estimates the carbon cycle after implementing a photosynthesis model into SSiB (Zhan et al., 2003). The TRIFFID dynamic global vegetation model (DGVM) was coupled to SSiB4 to calculate vegetation dynamics, including plant distribution and soil carbon. Currently, SSiB4 provides estimates of plant carbon fluxes, including net plant photosynthesis assimilation rate, autotrophic respiration rate, and other surface conditions, such as soil moisture and canopy temperature for TRIFFID. The TRIFFID model can then calculate LAI, plant height, fractional plant coverage, and surface aerodynamic resistance for SSiB4 based on the new plant state. The coupled SSiB4/TRIFFID analysis is able to divide the global terrestrial ecosystems into seven PFTs, including evergreen broadleaf trees, deciduous broadleaf trees, needleleaf broadleaf trees, C_3 grasses, C_4 plants, shrubs, and the tundra biome.

2.1.1. *Leaf phenology*

Leaf mortality rates ($\gamma_{\rm lm}$) are assumed to be a function of canopy temperature (T) and soil moisture availability (θ); $\gamma_{\rm lm}$ increases linearly from a minimum value of γ_0 when the leaf temperature and soil moisture availability drop below a threshold value:

$$\gamma_{\rm lm}=\begin{cases}\gamma_0, & T>T_{\rm off}\ \text{and}\ \theta>\theta_{\rm off}\\ \gamma_0\left(1+\varepsilon_{\rm dt}\left(T_{\rm off}-T\right)\varepsilon_{\rm dm}\left(\theta_{\rm off}-\theta\right)\right), & T\leqslant T_{\rm off}\ \text{or}\ \theta\leqslant\theta_{\rm off}\end{cases}. \tag{1}$$

Phenological status (p) is introduced to describe the seasonal variability of actual LAI (L). When the daily mean value of leaf turnover, as given by Eq. 1, exceeds twice its minimum value, leaves are dropped as a constant ($\gamma_{\rm p}$). Budburst occurs at the same rate when $\gamma_{\rm lm}$ drops back below this threshold, and "full leaf" is approached asymptotically thereafter

$$L=pL_{\rm b}\,, \tag{2}$$

$$\frac{{\rm d}p}{{\rm d}t}=\begin{cases}-\gamma_{\rm p} & \gamma_{\rm lm}>2\gamma_0\\ \gamma_{\rm p}\left(1-p\right) & \gamma_{\rm lm}\leqslant 2\gamma_0\end{cases}. \tag{3}$$

Balanced LAI ($L_{\rm b}$) responds to changes in the vegetation carbon, but $L_{\rm b}$ does not have an explicit seasonal cycle, which is related to a high carbon density and canopy height

$$W_{\rm c}=a_{\rm wl}(L_{\rm b})^{b_{\rm wl}}\,, \tag{4}$$

$$h=\frac{W_{\rm c}}{a_{\rm ws}\eta_{\rm sl}}\left(\frac{a_{\rm wl}}{W_{\rm c}}\right)^{1/b_{\rm wl}}. \tag{5}$$

2.1.2. *Vegetation carbon fluxes*

The calculations of vegetation carbon fluxes are based on the $A_{\rm n}-g_{\rm s}$ model, which is developed by Collatz et al. (1991). An additional direct soil moisture dependence is introduced to describe the impacts of water stress (Cox et al., 1998). The net leaf photosynthesis ($A_{\rm n}$) and stomatal conductance ($g_{\rm s}$) to water vapor are written as:

$$A_{\rm n}=\beta\frac{g_{\rm s}}{1.6}\frac{c_{\rm c}-c_{\rm i}}{p_{\rm sf}}\,, \tag{6}$$

$$\beta=\begin{cases}1 & \theta>\theta_{\rm c}\\ \dfrac{\theta-\theta_{\rm w}}{\theta_{\rm c}-\theta_{\rm w}} & \theta_{\rm w}<\theta\leqslant\theta_{\rm c}\\ 0 & \theta\leqslant\theta_{\rm w}\end{cases}. \tag{7}$$

The leaf to canopy scaling factor (Π) is used to calculate the net canopy photosynthesis ($A_{\rm c}$)

$$A_{\rm c}=A_{\rm n}\Pi\,, \tag{8}$$

$$\Pi=\frac{VN(1-e^{-\frac{\bar{k}L}{VN}})}{\bar{k}}. \tag{9}$$

The expression of gross primary productivity (GPP) is written as:

$$\mathrm{GPP} = 0.012\,(A_c + \beta R_{dc})\ . \tag{10}$$

The symbols in the above equations are listed in Appendix A.

2.2. *Data*

2.2.1. *Meteorological forcing data*

In this study, we employed two separate meteorological forcing datasets created by different universities in our simulations over the TP. Their details are as follows. The PMFD version 1 for the land surface model (Sheffield et al., 2006) combines a suite of global observation-based datasets from the National Center for Environmental Prediction and the National Center for Atmospheric Research (NCEP-NCAR) reanalysis data from 1948–2007. This dataset has a spatial resolution of 1° × 1° and a temporal interval of 3 h. These data have been widely used to drive models of terrestrial hydrologic and ecological processes to study seasonal and interannual variability.

The CMFD is the first high spatial-temporal resolution gridded near-surface meteorological dataset over China, developed by the hydrometeorological research group at the ITPCAS. This dataset was created by combining ground-based observations with several gridded datasets from remote sensing and reanalysis, including daily site data from the China Meteorological Administration (CMA), China Meteorological Data Service Center (CMDC), sub-daily site data from the National Oceanic and Atmospheric Administration (NOAA), National Centers for Environmental Information (NCEI), TRMM 3B42 satellite precipitation data, and Global Land Data Assimilation System data (GLDAS). The spatial resolution was 1° × 1°, and the temporal interval was 3 h from 1979 to 2018. The CMFD dataset is widely used forcing data for land surface models because of its high resolution and consistent quality.

In addition, a multi-year mean climatology with a 3-h interval from 1 January to 31 December of the PMFD and CMFD was generated to drive the quasi-equilibrium simulation.

2.2.2. *Validation data*

In this study, we used the Global Land Surface Satellite (GLASS) LAI (Xiao et al., 2014) to assess the spatial distribution and variation of simulated LAI, which is widely used because of its reliability, spatial integrity, and temporal consistency in global change and climate studies (Zhang et al., 2016; Liang et al., 2020). This dataset was generated from the Moderate Resolution Imaging Spectroradiometer (MODIS) reflectance data and the Advanced Very-High-Resolution Radiometer (AVHRR) reflectance data and had a spatial resolution of 1 km and temporal resolution of eight days. We resampled the GLASS LAI from 1982 to 2007 to a spatial resolution of 1° and monthly temporal resolution intended to match the simulated LAI.

The GPP from the FLUXNET model tree ensemble (MTE) was used to evaluate the simulated GPP. This dataset was upscaled to the observed carbon dioxide flux from a global network of eddy covariance towers using a machine learning approach MTEs, programmed to predict site-level GPP based on FLUXNET site data, remote sensing indices, climate and meteorological data, and land-use information (Jung et al., 2017). The dataset was created at a spatial resolution of 0.5°, and a monthly temporal resolution from 1982–2011. It was widely used to evaluate GPP simulations from LSMs, notwithstanding potential errors in the data products (Alemohammad et al., 2017). The FLUXNET-MTE GPP was resampled to 1°, the same as the GLASS LAI. In addition, we chose the monthly average air temperature and precipitation at 21 observation stations located in the TP to evaluate the quality of PMFD and CMFD.

2.3. *evaluation metrics.*

The root-mean-square error (RMSE) and correlation coefficient (R) are the metrics used to evaluate the simulated results, which are calculated as follows:

$$R = \frac{\sum_{i=1}^{N}(M_i - \overline{M})(O_i - \overline{O})}{\sqrt{\sum_{i=1}^{N}(M_i - \overline{M})^2}\sqrt{\sum_{i=1}^{N}(O_i - O)^2}}\ , \tag{11}$$

$$\mathrm{RMSE} = \sqrt{\frac{\sum_{i=1}^{N}(M_i - O_i)^2}{N}}\ , \tag{12}$$

where M_i and O_i are the simulation and observation values, respectively, and $\overline{M}$ and $\overline{O}$ are the means of the simulation and observation values, respectively.

2.4. *Experimental design*

2.4.1. *Equilibrium simulations*

Quasi-equilibrium simulation runs are needed prior to a realistic simulation run to obtain a stable vegetation state in the dynamic vegetation model (DVM) (Table 1). To simulate the spatial distribution of vegetation on the TP accurately, we updated the SSiB vegetation map and table with a multi-source integrated Chinese land cover (MICLCover) map (Ran et al., 2012), which is resampled to the corresponding spatial resolution. In addition, climatological forcing data and 1979 atmospheric CO_2 concentrations were used to drive SSiB4/TRIFFID for 100 years to get a stable vegetation state in a quasi-equilibrium. The quasi-equilibrium run initialized the vegetation conditions for subsequent model runs.

2.4.2. *Realistic simulations*

We conducted three experiments with SSiB4/TRIFFID to assess the performance of realistic and high-resolution meteorological forcing data on the LAI and GPP simulations and used the vegetation conditions produced by the quasi-equilibrium runs and updated atmospheric CO_2 concentrations. We used the PMFD and the upscaled CMFD to drive the model, labeled "PMFD 1D" and "CMFD 1D", to investigate the performance of the two meteorological forcing datasets. They have the same spatial resolution of 1° × 1°. We

Table 1. Experimental Design.

	100-year equilibrium simulation			Realistic simulation		
	CO_2 concentration	Initial vegetation condition	Atmospheric forcing	CO_2 concentration	Initial vegetation condition	Atmospheric forcing
PMFD 1D	Fixed CO_2 concentration at 1979 level	Updating vegetation mapwith Chinese vegetation map	3-hourly climatological Princeton atmosphericforcing data from 1979 to 2007, 1 degree	Transient CO_2 for the period of 1979–2007	The vegetation Condition-sreproduced by the 100-year equilibrium runs	Transient 3-hourly Princeton atmospheric forcing data from 1979 to 2007, 1 degree
CMFD 1D			3-hourly climatological CMFD from 1979 to 2007, 1 degree			Transient 3-hourly CMFD from 1979 to 2007, 1 degree
CMFD 0.1D			3-hourly climatological CMFD from 1979 to 2007, 0.1 degree			Transient 3-hourly CMFD from 1979 to 2007, 0.1 degree

also used the high spatial resolution CMFD to drive SSiB4/TRIFFID, labeled "CMFD 0.1D", and explored how different spatial resolutions would affect the vegetation simulation. Two historical meteorological forcing datasets were used to drive SSiB4/TRIFFID to simulate the 1979–2007 period.

3. Results and analyses

3.1. *Intercomparison and evaluation of the two atmospheric forcing datasets*

Land Surface Models (LSMs) are driven by atmospheric forcing data. Air temperature, precipitation, and solar radiation play important roles in simulating the vegetation growth in the model (Ren et al., 2021). Therefore, we compared these three atmospheric forcing variables between PMFD and CMFD. Figure S1(in the electronic supplementary materials, ESM) shows the spatial patterns of downward shortwave radiation averaged over 1979–2007 from PMFD and CMFD in the TP. It is evident that the spatial patterns of shortwave radiation were similar for the two datasets. The multi-year averaged values of shortwave radiation from CMFD and PMFD were 216.72 W m^{-2} and 207.81 W m^{-2}, respectively. In addition, the seasonal cycles of shortwave radiation agreed well between CMFD and PMFD, although the values of CMFD were higher from April to September (Fig. S2 in the ESM).

The spatial patterns and seasonal air temperature cycles were in good agreement between CMFD and PMFD (Figs. S3 and S4 in the ESM). We also compared the air temperature of CMFD and PMFD against the observations from 21 sites over the TP (Fig. S5). The statistical metrics (Table S1 in the ESM) show that both datasets are close to the site-observed data. However, the RMSE and R^2 were improved for the CMFD air temperature.

Figure 1 shows the spatial patterns of monthly averaged precipitation over 1979–2007. Spatial patterns of precipitation of CMFD and PMFD were different from each other. The precipitation of CMFD increased from southeast to northeast, which was consistent with the distribution of vegetation. However, the precipitation of PMFD was much higher in the southwestern TP. From the perspective of seasonal cycling, the precipitation of PMFD was much higher than that of CMFD in summer (Fig. S6 in the ESM). We evaluated the precipitation of PMFD and CMFD based on the in-situ station data. The statistical metrics show that monthly-averaged precipitation of PMFD was overestimated by more than 10 mm $month^{-1}$ in 19 of the 21 sites. However, the biases were significantly reduced for CMFD, with a lower RMSE and a higher R^2 for CMFD precipitation.

3.2. *Influence of different atmospheric forcing datasets on simulations of vegetation dynamics*

3.2.1. *Spatial patterns of LAI*

LAI is defined as half the total green leaf area per unit of horizontal ground surface area. As a measure of canopy foliage, LAI is related to a range of biochemical processes, such as photosynthesis, transpiration, and energy exchanges.

We evaluated the spatial patterns of the averaged-seasonal and annual LAI from 1982–2007 over the TP. The mean annual GLASS LAI shows that large LAI values are found over the southeastern and eastern TP, where forests and alpine meadows dominate the vegetation; smaller LAI values are found over northwestern and western TP (c1 in Fig. 2). Large seasonal variations of LAI in the eastern TP are apparent, with the area of large LAI values (greater than 1.5) ranging from 15.3% (summer) to 6.8% (spring). In contrast, the LAI in the southern TP varies little with the seasons (c2–c4 in Fig. 2). The two simulations with SSiB4/TRIF-

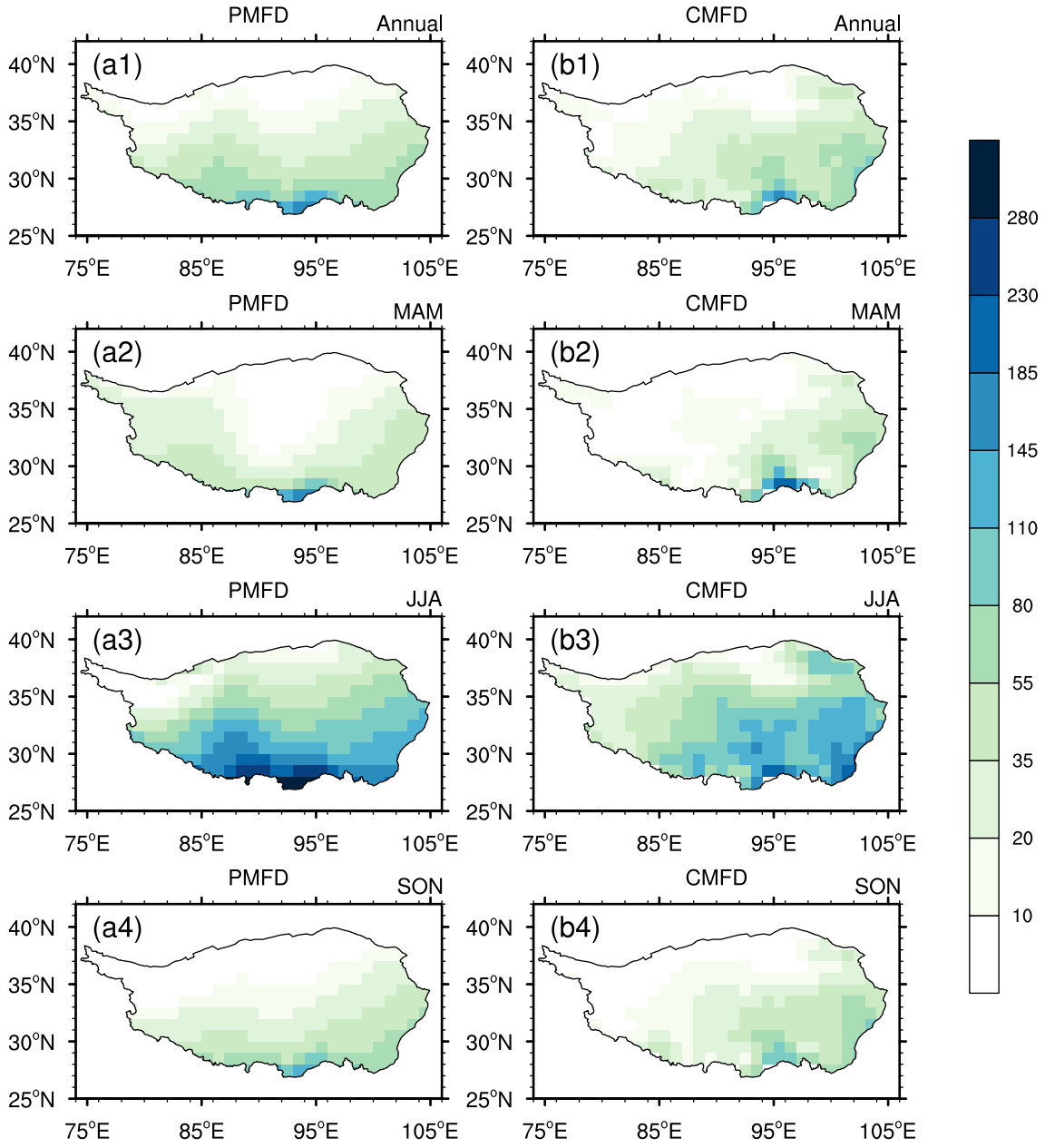

Fig. 1. Spatial patterns of multi-year averaged annual and seasonal (MAM, JJA, SON) precipitation during 1979–2007. (a1–a4) PMFD, (b1–b4) CMFD; Units: mm month^{-1}.

FID forced by the PMFD and upscaled CMFD reproduced similar spatial patterns and seasonal variations of LAI over the TP with GLASS LAI (a1–a4, b1–b4 in Fig. 2). In contrast, there was an overestimation of simulated LAIs against the GLASS LAI. Figure 3 shows the differences in mean annual and seasonal LAIs differences between PMFD 1D, CMFD 1D, and GLASS. LAI simulations in PMFD 1D were overestimated (up to 60% in summer) in most regions of the TP. Substantial improvements were seen with CMFD 1D with reduced LAI, especially in the western and eastern regions of the TP. The annual averaged LAI bias over the entire TP reduced from 0.39 to 0.15, and the RMSE reduced by 24.3% (from 0.70 to 0.53). The seasonal average LAI decreased substantially, with the bias decreasing by 52.1%–71.3% (Table 2). Thus, the LAI over TP can be simulated more reasonably by upscaled CMFD at the same spatial resolution.

3.2.2. *Spatial patterns of GPP*

Gross primary production (GPP) is an important flux variable describing land-atmosphere carbon exchange. In this subsection, GPP simulations from 1982 to 2007 were compared and evaluated using observation-based GPP data over the TP.

Figure 4 displays the spatial patterns of the multi-year averaged annual and seasonal GPP of the PMFD 1D (a1–a4), CMFD 1D (b1–b4), and observation (c1–c4) from 1982 to 2007. Large spatial variabilities of annual mean

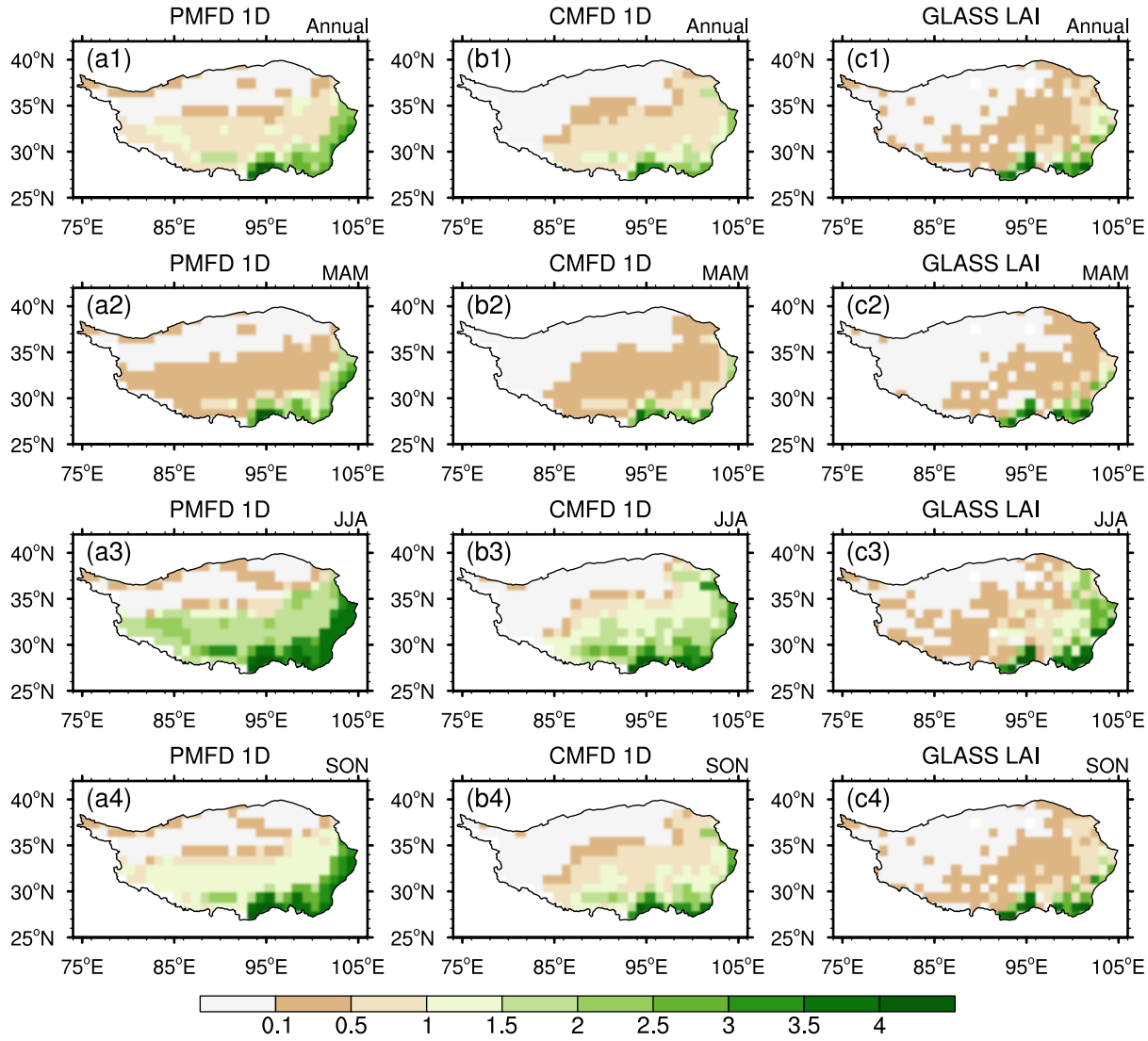

Fig. 2. Spatial patterns of multi-year averaged annual and seasonal (MAM, JJA, SON) LAI during 1982–2007. (a1–a4) PMFD 1D, (b1–b4) CMFD 1D, (c1–c4) GALSS LAI; Units: m^2 m^{-2}.

GPP were found in the FLUXNET-MTE datasets, with an increasing gradient from the northwest to the southeast (c1 in Fig. 4). The mean annual GPP is higher than 90 gC m^{-2} $month^{-1}$ in the southern TP region. In contrast, the mean annual GPP was generally lower than 10 gC m^{-2} $month^{-1}$ in the northwestern areas, dominated by desert, bare soil, and sparsely vegetated alpine steppe. Strong seasonal fluctuations of FLUXNET-MTE GPP are quite obvious in the eastern and southeastern regions of the TP. The area where GPP values were greater than 30 gC m^{-2} $month^{-1}$ ranges from 7.9% (in spring) to 37.5% (in summer). Figure 5 (a1) shows unrealistic mean annual GPP values exist in the southwestern region in the PMFD 1D (ranging from 30 to 50 gC m^{-2} $month^{-1}$) where the vegetation is very sparse, contrary to its observed value (lower than 10 gC m^{-2} $month^{-1}$). The mean seasonal GPP has consistent results, and the overestimation is much higher (over 65 gC m^{-2} $month^{-1}$) in the summer (a3 in Fig. 5). The overestimation is reduced to some extent on the southwestern TP in CMFD 1D (b1–b4 in Fig. 5). However, the decrease in simulated GPP in CMFD 1D on the eastern TP is excessive, and the GPP simulation is underestimated. Table 3 shows the comparisons between the simulated GPP and FLUXNET GPP data. The bias of annual-averaged monthly GPP simulations in the CMFD 1D is –0.34 gC m^{-2} $month^{-1}$, which is significantly lower than that in the PMFD 1D (9.95 gC m^{-2} $month^{-1}$), a reduction of 50.4% on percentage bias. The RMSE of annual-averaged monthly GPP simulations in the CMFD 1D decreased by 20.5% (from 19.7 gC m^{-2} $month^{-1}$ to 15.66 gC m^{-2} $month^{-1}$). In addition, the spatial correlation coefficient (SCC) of the GPP simulation with upscaled CMFD increased by 4.8%. The improvement of GPP simulations with upscaled CMFD is more significant on the seasonal scale, with a reduction in RMSE by 35.4% (in autumn) and an increase in SCC by 16.7% (in summer).

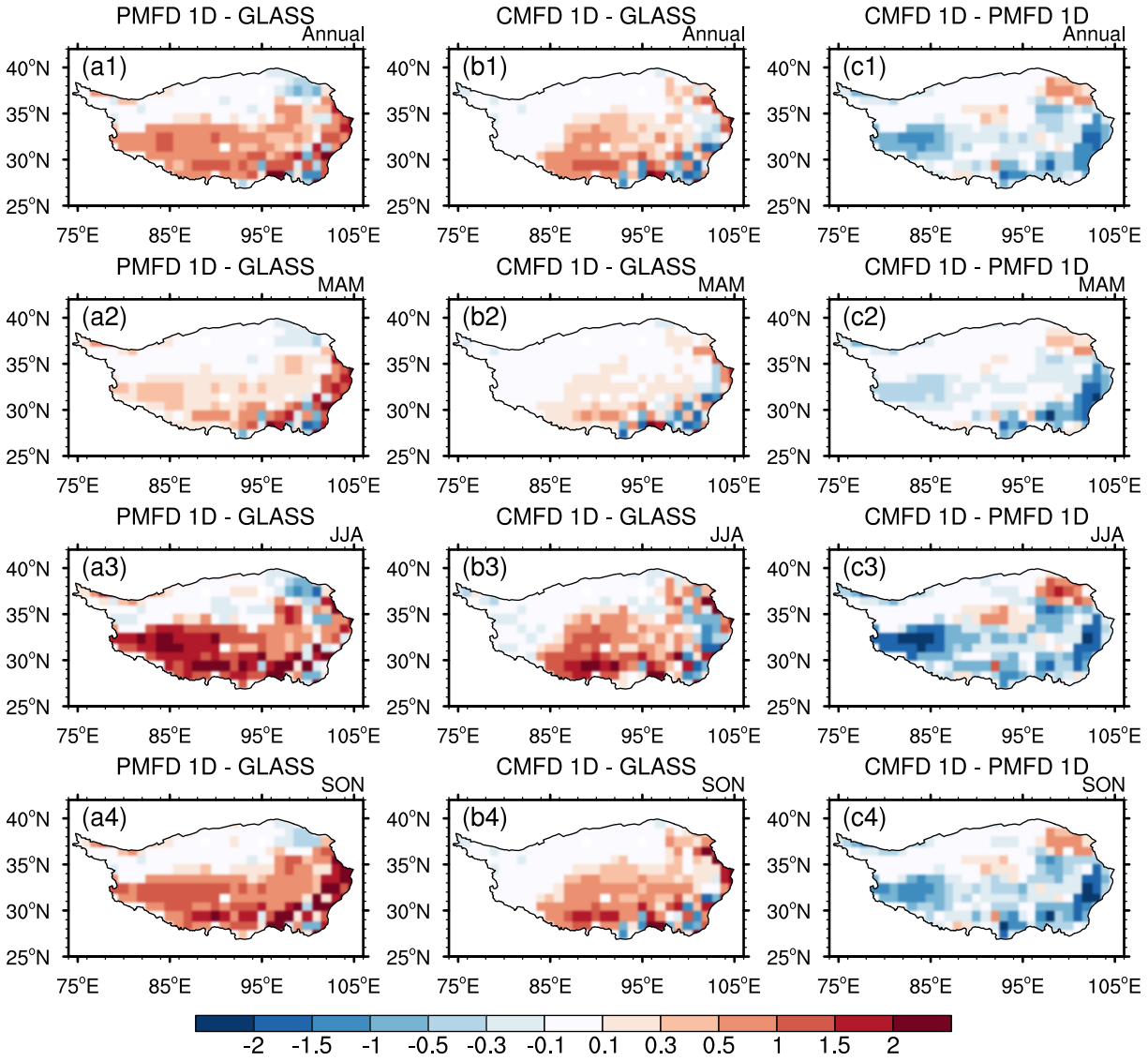

Fig. 3. Differences in multi-year averaged annual and seasonal LAI between 1982–2007. (a1–a4) PMFD 1D minus GLASS, (b1–b2) CMFD 1D minus GLASS, (c1–c4) CMFD 1D minus PMFD 1D; units: m^2 m^2.

Table 2. Seasonal and annual averaged LAI statistics for the comparison between the model simulations and observation.

	LAI (m^2 m^{-2})															
	MAM (Spring)				JJA (Summer)				SON (Autumn)				ANN (Annual)			
	MEAN	BIAS	RMSE	SCC	MEAN	BIAS	RMSE	SCC	MEAN	BIAS	RMSE	SCC	MEAN	BIAS	RMSE	SCC
GLASS	0.33	–	–	–	0.71	–	–	–	0.45	–	–	–	0.44	–	–	–
PMFD 1D	0.54	0.21 (63.6%)	0.53	0.65*	1.42	0.71 (100%)	1.16	0.70*	1.07	0.62 (137.8%)	0.96	0.68*	0.83	0.39 (88.6%)	0.70	0.77*
CMFD 1D	0.36	0.03 (9.1%)	0.44	0.59*	1.05	0.34 (47.9%)	0.81	0.75*	0.75	0.30 (66.7%)	0.67	0.71*	0.59	0.15 (34.1%)	0.53	0.77*
CMFD 0.1D	0.38	0.05 (15.2%)	0.41	0.78*	1.03	0.32 (45.1%)	0.72	0.81*	0.75	0.30 (66.7%)	0.64	0.74*	0.60	0.16 (36.1%)	0.49	0.81*

* indicates significant values, $p < 0.05$, in Student-t test. MAM, JJA, SON, ANN represent spring, summer, autumn, and annual, respectively. RMSE and SCC represent root-mean-square error and spatial correlation coefficient.

3.2.3. *Temporal patterns of LAI and GPP*

The climate change-related regional warming and precipitation increases influence the vegetation growth and productivity on the spatial scale (Zhu et al., 2016). This section evaluates the efficacy of different meteorological forcing datasets to predict LAI and GPP variability trends.

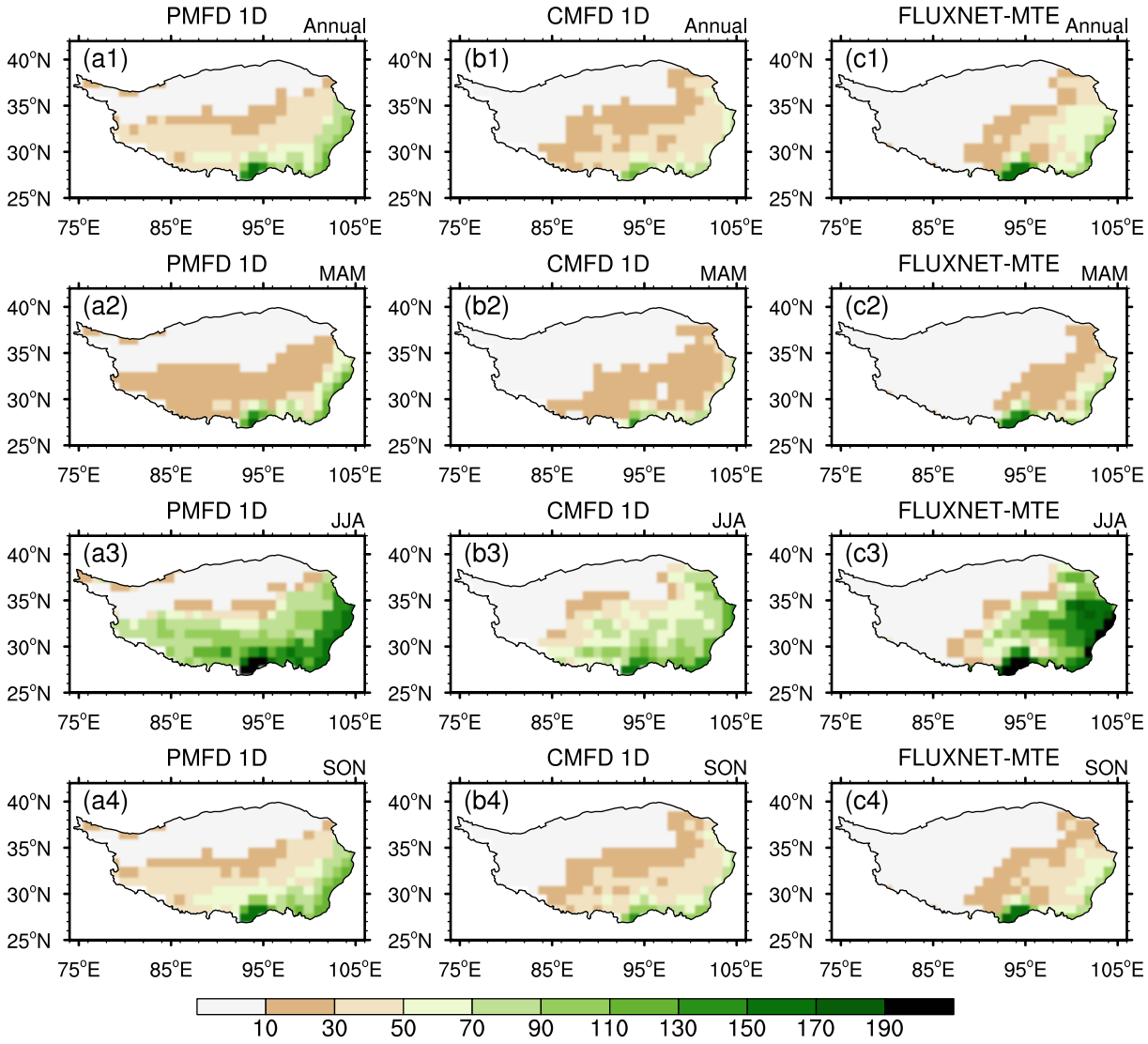

Fig. 4. Spatial patterns of multi-year averaged annual and seasonal (MAM, JJA, SON) GPP during 1982–2007. (a1–a4) PMFD 1D , (b1–b4) CMFD 1D, (c1–c4) FLUXNET-MTE; Units: gC m^{-2} $month^{-1}$.

Figure 6 shows the comparison of annual mean LAI between the simulations and satellite data from 1982 to 2007. Both PMFD 1D and CMFD 1D captured the variations of LAI. The simulation with upscaled CMFD is close to the observed value, with a 56.4% decrease in RMSE and a 5.9% increase in the temporal correlation coefficient (TCC) (Table 4). In addition, both simulated LAIs show a significant greening trend on the TP. However, there is an obvious difference between simulated and satellite-derived LAI trends. The CMFD 1D has the largest trend of LAI, with an annual increase of 0.01. The right-hand column in Fig. 6 gives the mean seasonal cycle of simulated and satellite-derived LAI. The simulation of LAI in CMFD 1D shows a lower amplitude in summer, which is closer to the GLASS LAI. To further investigate the improvement of temporal simulation with upscaled CMFD, we made a scatterplot comparison between the monthly simulated LAI and GLASS LAI (Fig. 7). The simulation of LAI in CMFD showed improvement, evidenced by an RMSE and bias that were reduced by 46.2% and 61.5%, respectively.

We also compared the simulated and observation-based annual GPP time series over the TP. Figure 8 shows the temporal patterns of annual monthly mean GPP from 1982–2007. The trend and the annual average values of GPP simulations with different meteorological forcing datasets have noticeable differences. The CMFD 1D improved upon the performance of the GPP simulation by a large margin, with a reduction of RMSE by 81.6% and an increase in TCC by 21.1%. Both simulated GPPs suggest that the ecosystems' ability to fix carbon is increasing. The trend of simulated GPP in the CMFD 1D is 3.21 gC m^{-2} yr^{-2} which is the larger among the two simulations and FLUXNET GPP data (Table 4). The comparison of the mean seasonal cycle of simulated GPP to the observation-based GPP (right-hand side of Fig. 8) reveals that the CMFD 1D decreased the GPP in the simulation excessively in the summer, which may be directly influenced by the variation in LAI. Besides, the CMFD 1D largely reduces the GPP estimates from

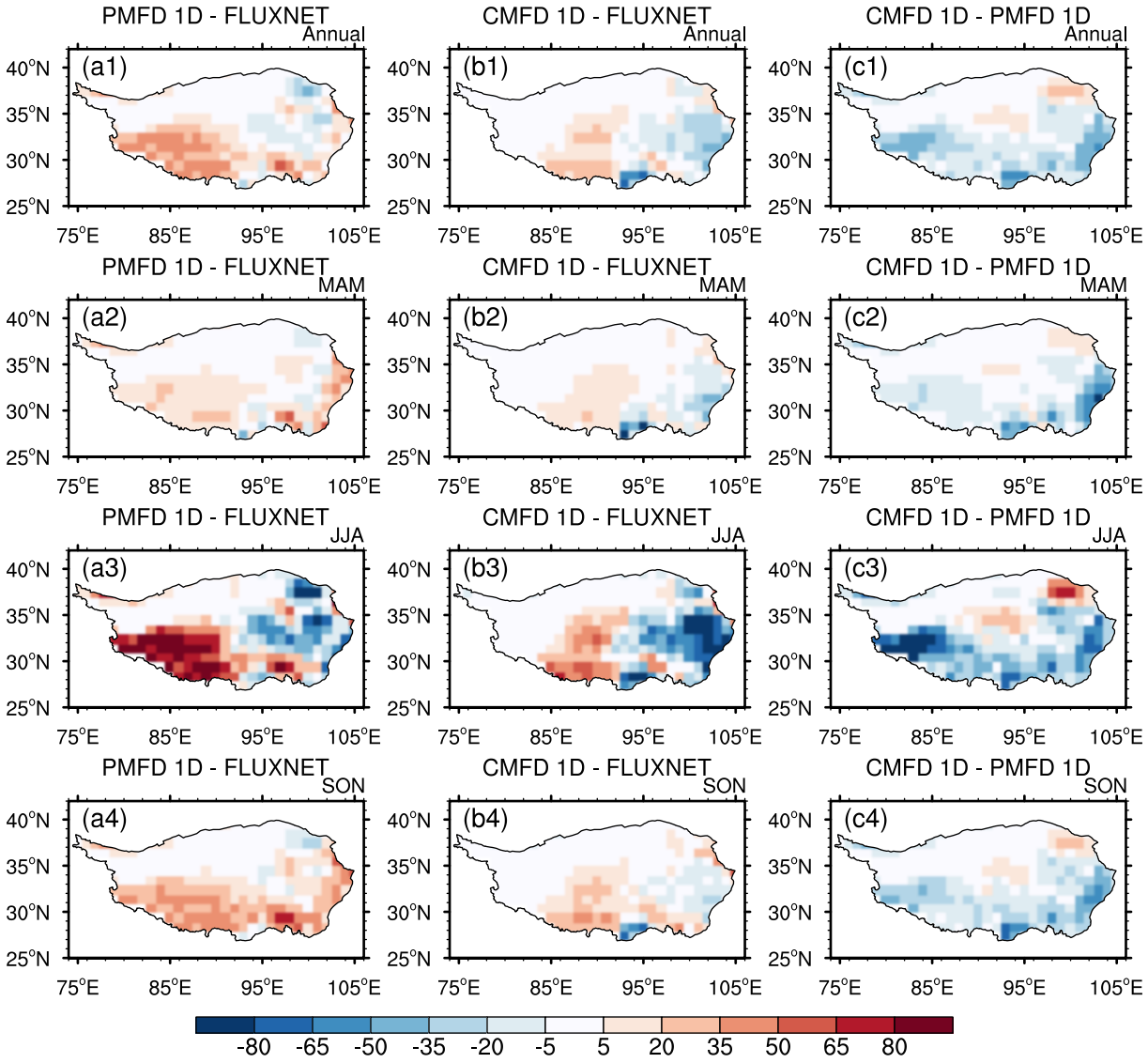

Fig. 5. Difference between multi-year averaged annual and seasonal GPP during 1982–2007. (a1–a4) PMFD 1D minus FLUXNET, (b1–b2) CMFD 1D minus GLASS, (c1–c4) CMFD 1D minus PMFD 1D; units: gC m^{-2} $month^{-1}$.

Table 3. Seasonal and annual averaged GPP statistics for the comparison between the model simulations and observation.

	GPP (gC $m^{-2}$$month^{-1}$)															
	MAM (Spring)				JJA (Summer)				SON (Autumn)				ANN (Annual)			
	MEAN	BIAS	RMSE	SCC	MEAN	BIAS	RMSE	SCC	MEAN	BIAS	RMSE	SCC	MEAN	BIAS	RMSE	SCC
FLUXNET MTE	12.09	–	–	–	48.34	–	–	–	17.59	–	–	–	20.44	–	–	–
PMFD 1D	19.25	7.16 (59.2%)	13.39	0.79*	61.08	12.74 (26.4%)	44.85	0.72*	33.04	15.45 (87.8%)	23.36	0.75*	30.39	9.95 (48.7%)	19.70	0.83*
CMFD 1D	11.58	−0.51 (4.2%)	12.86	0.81*	42.16	−6.18 (−12.8%)	36.30	0.84*	21.73	4.14 (23.5%)	15.09	0.80*	20.10	−0.34 (−1.7%)	15.66	0.87*
CMFD 0.1D	11.89	−0.20 (−1.7%)	11.27	0.91*	39.84	−8.50 (−17.6%)	34.38	0.88*	20.92	3.33 (18.9%)	13.08	0.84*	19.41	−1.03 (−5.0%)	14.17	0.90*

As in Table 2 except for GPP.

364.7 to 241.2 gC m^{-2} yr^{-1}, which is much closer to the observed value (245.31 gC m^{-2} yr^{-1}). The scatterplot comparisons of monthly simulated GPP and FLUXNET-MTE GPP (Fig. 9) confirm a good performance of the GPP simulation with an upscaled CMFD on a monthly timescale. Generally, a more realistic CMFD improves the simulations of LAI

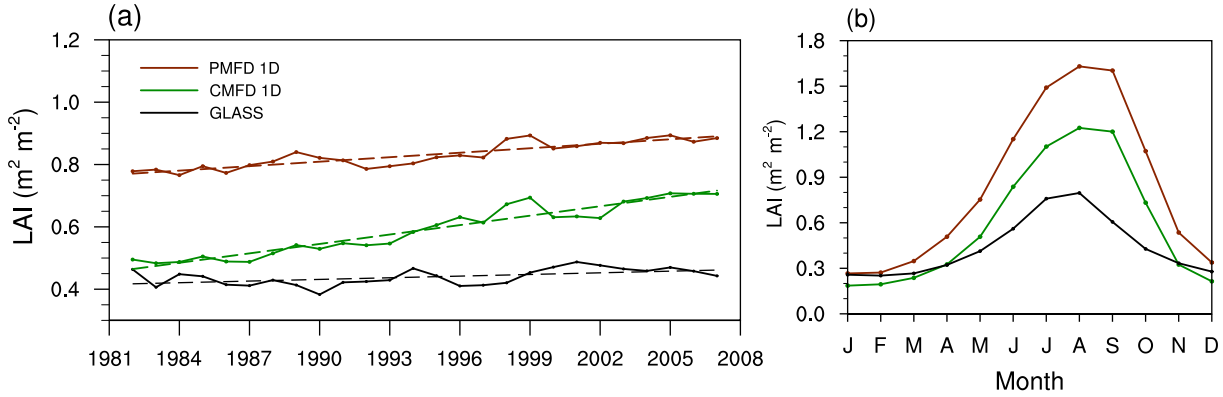

Fig. 6. Comparison of time series of LAI between simulations and observation. The right-hand column shows the corresponding multi-year mean seasonal cycle and the monthly average.

Table 4. Statistics for the comparison between simulated and observation-based LAI and GPP.

	LAI (m^2 m^{-2})			GPP (gC m^{-2} yr^{-1})		
	Trend (yr^{-1})	RMSE (m^2 m^{-2})	TCC	Trend (gC m^{-2} yr^{-2})	RMSE (gC m^{-2} yr^{-1})	TCC
OBS	0.002*	–	–	0.73*	–	–
PMFD 1D	0.005*	0.39	0.51*	1.78*	120.27	0.51*
CMFD 1D	0.010*	0.17	0.54*	3.21*	22.10	0.62*

and GPP over the TP, regardless of spatial or temporal scales.

3.3. *Influence of the improved spatial resolution on simulations of vegetation dynamics*

The spatial resolution of atmospheric forcing data is an important factor that affects the performance of simulation in LSMs (Zhao and Li, 2015). To explore the influence of spatial resolution of atmospheric forcing data on the simulations of LAI and GPP, we forced the SSiB4/TRIFFID with high spatial resolution CMFD (0.1° × 0.1°), referred to as CMFD 0.1D.

3.3.1. *Leaf area index*

Figure 10 shows the comparisons of the annual and seasonal multi-year averages of LAI between CMFD 0.1D, CMFD 1D, and the observations during 1982–2007. The spatial patterns of annual and seasonal LAI bias in CMFD 0.1D were similar to those in CMFD 1D. The difference in annual and seasonal LAI simulations between CMFD 0.1D and CMFD 1D are shown in Fig. 10 (b1–b4). Compared to CMFD 1D, the RMSE of annual LAI in CMFD 0.1D is reduced by 7.5% (from 0.53 to 0.49), and the SCC increased by 5.2% (from 0.77 to 0.81). The improvements in LAI simulation with high spatial resolution CMFD are focused on the southwestern and eastern regions of the TP, with an area covering 21.5%. Improvement in LAI simulation during summer is quite obvious, with a 0.09 (11.1%) decrease in RMSE and 0.06 (8.0%) in SCC.

A Taylor diagram can quantify the performance of each run in simulating the annual- and seasonal-averaged LAI. Figure 11a gives multiple statistics of the simulated LAI. Higher values of SCC and decreased RMSE indicate a large

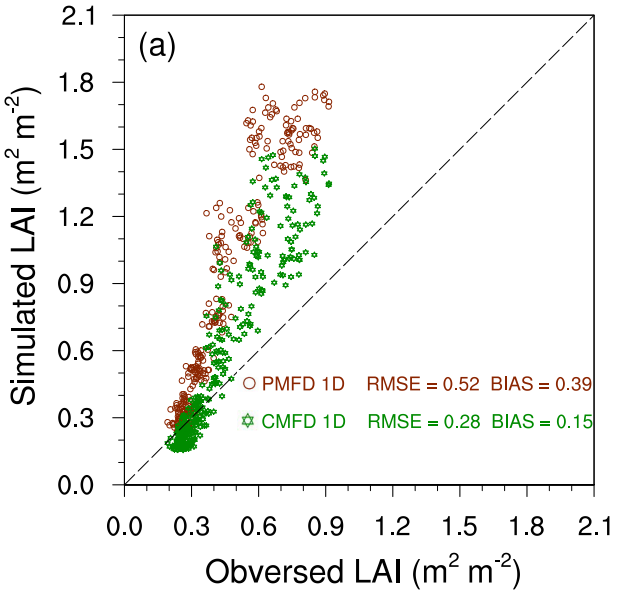

Fig. 7. Scatterplot comparison at a monthly scale between GLASS LAI and simulated LAI.

improvement in a simulated LAI simulation using a high-spatial-resolution CMFD. The improvements in an LAI simulation due to the improved spatial resolution of meteorological forcing data are secondary.

3.3.2. *Gross primary production*

We compared the spatial patterns of the multi-year averaged annual and seasonal GPP between CMFD 0.1D, CMFD 1D, and the observations from 1982 to 2007 (Fig. 12). The simulation in CMFD 0.1D underestimated the GPP in the eastern and southeastern regions and overestim-

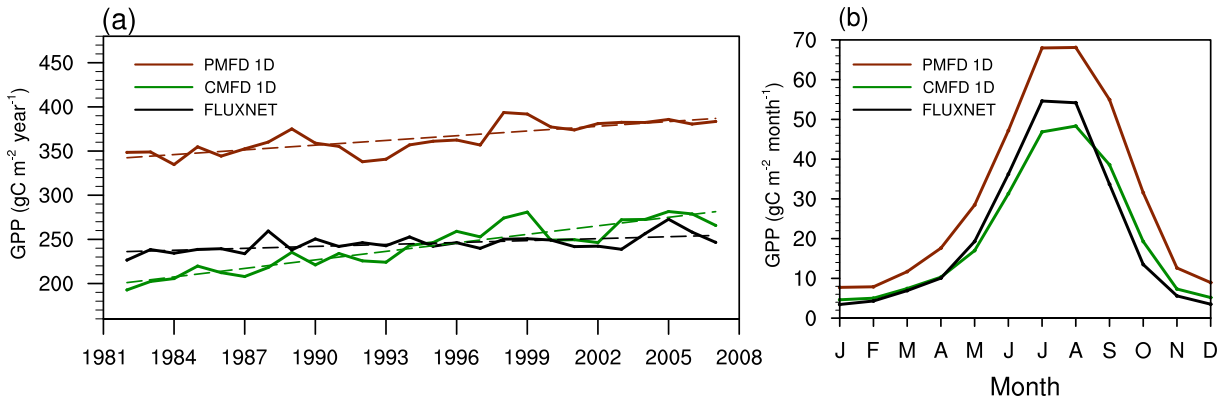

Fig. 8. Comparison of time series of GPP between simulations and observation. The right-hand column shows the corresponding multi-year mean seasonal cycle and the monthly average.

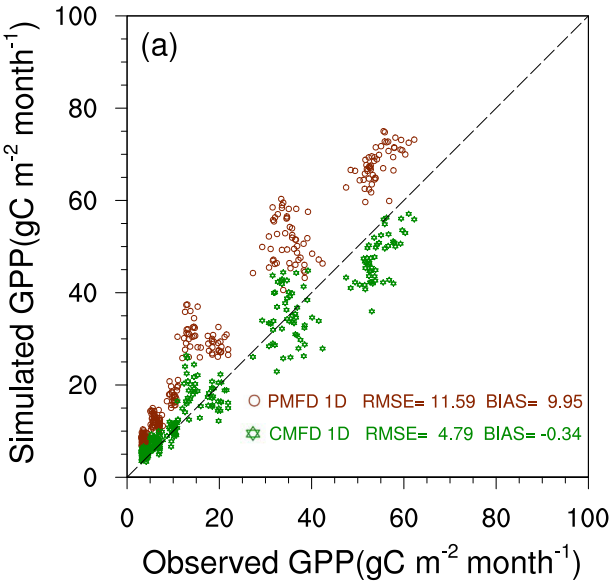

Fig. 9. Scatterplot comparison at a monthly scale between FLUXNET-MTE GPP and simulated GPP.

ated GPP in the southwestern regions over the TP, which is similar to CMFD 1D. The difference in the annual GPP simulation between CMFD 0.1D and CMFD 1D shows that CMFD 0.1D improves in regions where CMFD 1D has a simulated deviation. Compared to CMFD 1D, the RMSE was reduced by 9.5% (from 15.66 to 14.17 gC m^{-2} $month^{-1}$) and the SCC was increased by 3.4% (from 0.87 to 0.90). The improvement in the RMSE (SCC) of the seasonal GPP simulation ranges from 5.3% in summer (4.8% in summer) to 13.3% in autumn (12.3% in spring).

The Taylor diagram (Fig. 11b) assessed the performance of each run by simulating annual and mean seasonal GPP. The GPP simulations in CMFD 0.1D performed best with a large SCC and low RMSE. The improvement from PMFD 1D to CMFD 1D is more obvious than from CMFD 1D to CMFD 0.1D, which indicates that the improvement of the GPP simulation brought about by realistic atmospheric forcing data is larger than the improved spatial resolution of the atmospheric forcing data.

4. Discussion

Due to its unique geographical location, the vegetation on the TP is extremely sensitive to air temperature and precipitation during the growing season. According to previous studies, precipitation has been suggested to exert a larger impact on alpine meadow growth in the central-eastern TP (Zhang et al., 2018). Furthermore, it is revealed that the precipitation of the two datasets differs from one another (Fig. 1). The evaluation of precipitation from PMFD and CMFD against in-situ station data suggests a significant reduction in biases in the CMFD precipitation relative to PMFD precipitation, especially in the central-southwestern region of the TP. By comparing the precipitation differences and simulated vegetation dynamics between CMFD and PMFD, we found that the LAI and GPP simulations improved significantly in the areas with better precipitation forcing.

Soil moisture (SM) availability controls the seasonal variability of LAI by changing the leaf mortality rates (γ_{lm}) in Eq. 1), which determines the start and end of the growing season. In addition, the availability of soil moisture also impacts leaf photosynthesis, as is shown in Eq. 7. Therefore, SM is a crucial variable for the simulations of vegetation dynamics. We compared the simulated SM in the CMFD 0.1D and PMFD 1D runs with validation SM, established through a land data assimilation system (LDAS). Covering the period from 2002 to 2011, the LDAS-derived SM was produced by assimilating satellite brightness temperature data into an LSM and has been proven to be more accurate in the TP (Yang et al., 2020). Figure 13 (a1, b1, c1) displays the spatial patterns of simulated and validated SM averaged from 2003 to 2007. The LDAS-derived SM had a spatial pattern gradually decreasing from southeast to northwest on the TP, which was consistent with the vegetation distribution of the TP. However, the simulated SM of PMFD 1D run was higher than LDAS on the entire TP, especially in the southwestern region of the TP. Compared to the PMFD 1D run, the CMFD run performed better in simulating the spatial distribution of SM, evidenced by an SCC that increased by 29% (from 0.62 to 0.80) and an RMSE that was lowered by 36.5% (from 0.074 to 0.047). The latent heat flux (LH)

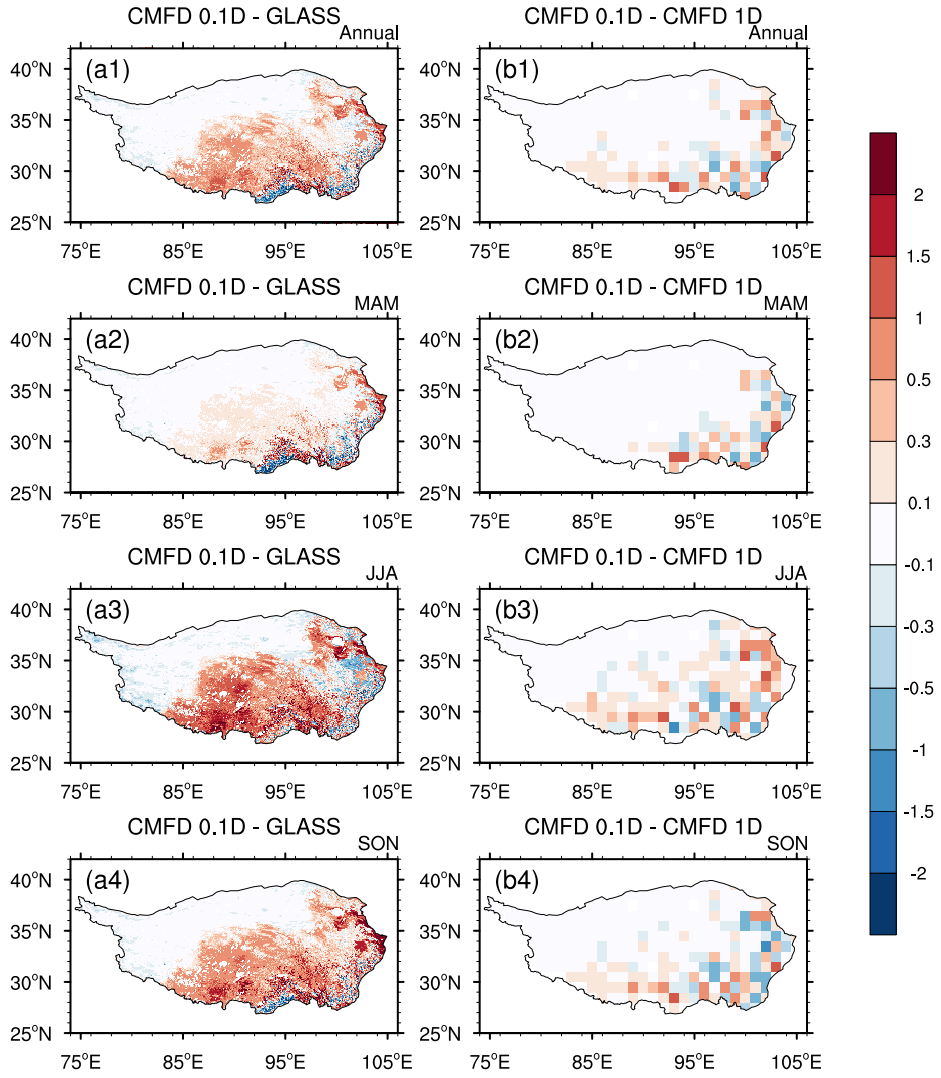

Fig. 10. (a1–a4) The difference between the multi-year averaged annual and seasonal LAI at 0.1-degree spatial resolution during 1982–2007. (b1–b4) The difference between the multi-year averaged annual and seasonal LAI simulations in CMFD 0.1D. Positive values represent improvement. Units: $m^2\ m^{-2}$.

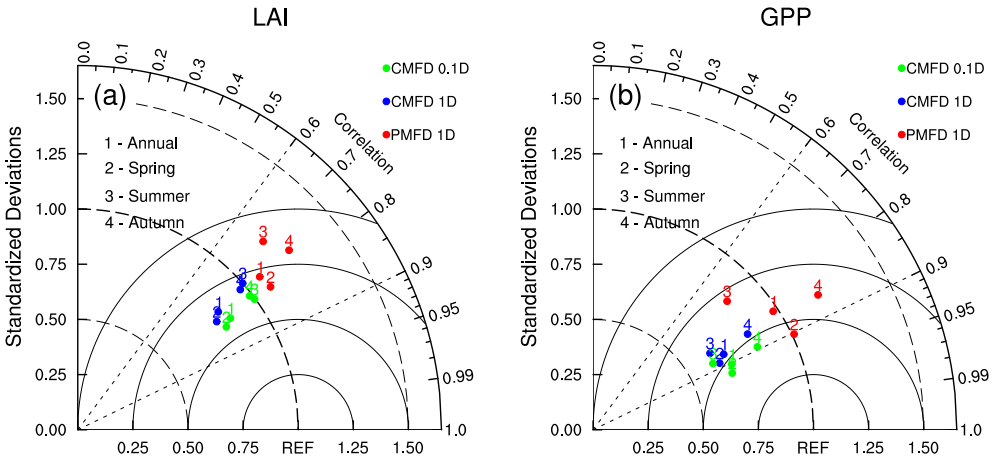

Fig. 11. Taylor diagram of the multi-year averaged annual and seasonal (a) LAI and (b) GPP simulations against the observed data over the TP. The annual, spring, summer, and autumn simulations are indicated by 1–4, respectively; the red, blue, and green marks denote the simulations from PMFD 1D, CMFD 1D, CMFD 0.1D, respectively.

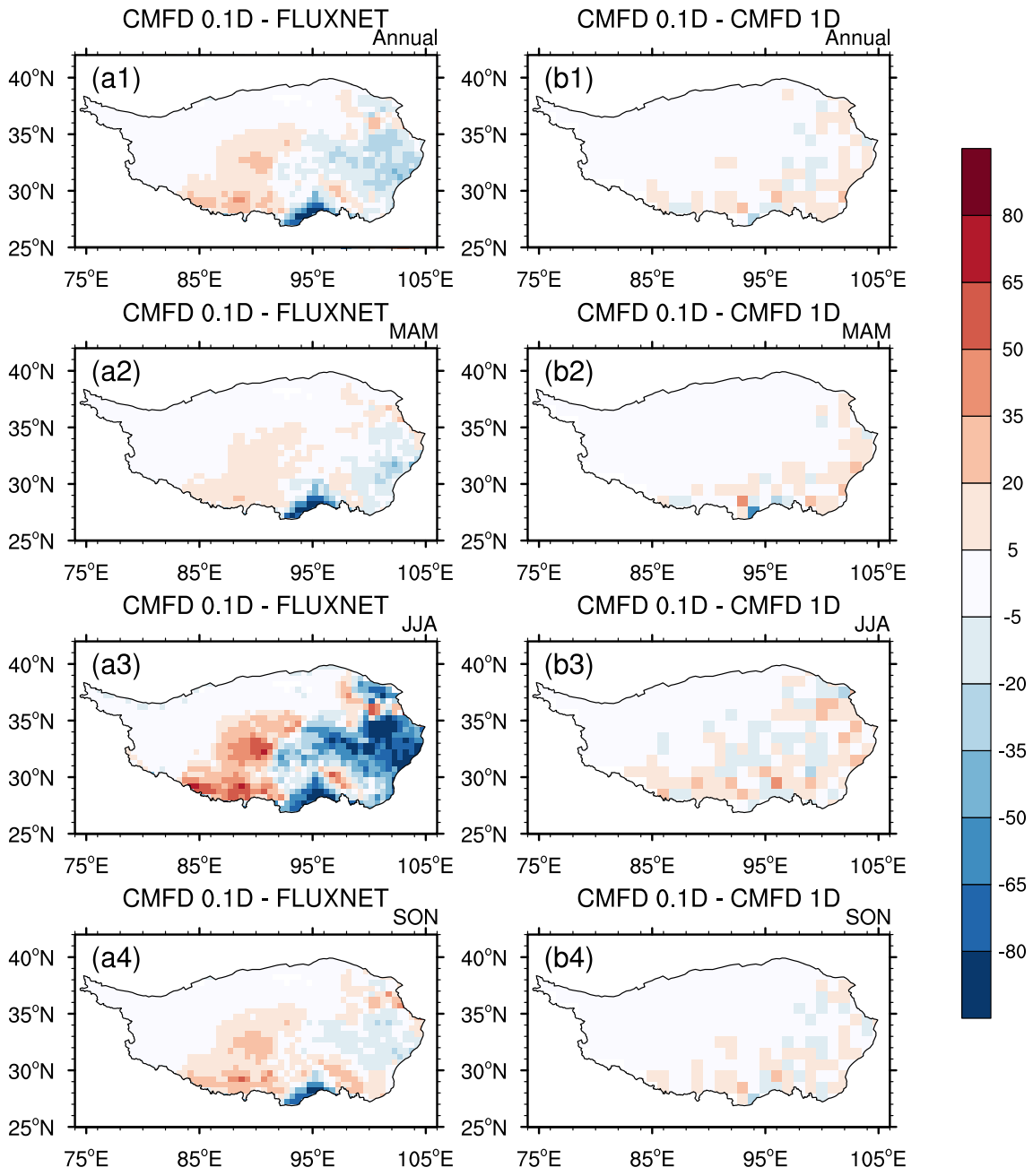

Fig. 12. (a1–a4) Difference between multi-year averaged annual and seasonal GPP at a 0.5-degree spatial resolution during 1982–2007. (b1–b4) The change in the multi-year averaged annual and seasonal GPP simulations in CMFD 0.1D. Positive values represent improvement. Units: gC m^{-2} $month^{-1}$.

simulation driven by CMFD also significantly improved (Figs.13 a2, b2, c2). Compared to FLUXNET-MTE data, the LH simulation driven by CMFD has a higher SCC and a lower RMSE compared to that of PMFD, with the SCC increasing from 0.18 to 0.84 and the RMSE decreasing to 6.1 from 11.6 Wm^{-2}. We also analyzed the spatial patterns of the two values of simulated sensible heat flux (SH) against FLUXNET-MTE (Figs.13 a3, b3, c3). Compared to PMFD, the SH simulations driven by CMFD also improved, with an RMSE reduction of 33.6%.

For the alpine grassland ecosystems of the TP, the SM plays an essential role in modeling leaf phenology and vegetation carbon fluxes. The improvement of precipitation in the CMFD improves the accuracy of the soil moisture simulation, and soil moisture further affects vegetation growth and ecosystem carbon fluxes by participating in the progression of leaf phenology and photosynthesis. Consequently, the correction of precipitation in the CMFD plays an essential role in the improvement of vegetation dynamics in SSiB4/TRIFFID model over the TP.

Additionally, the importance of moisture was also verified in the AVIM model. Lü and Ji (2002a) pointed out that the change in the dynamics and spatial distribution of NPP and LAI on the TP was controlled by both the moisture and

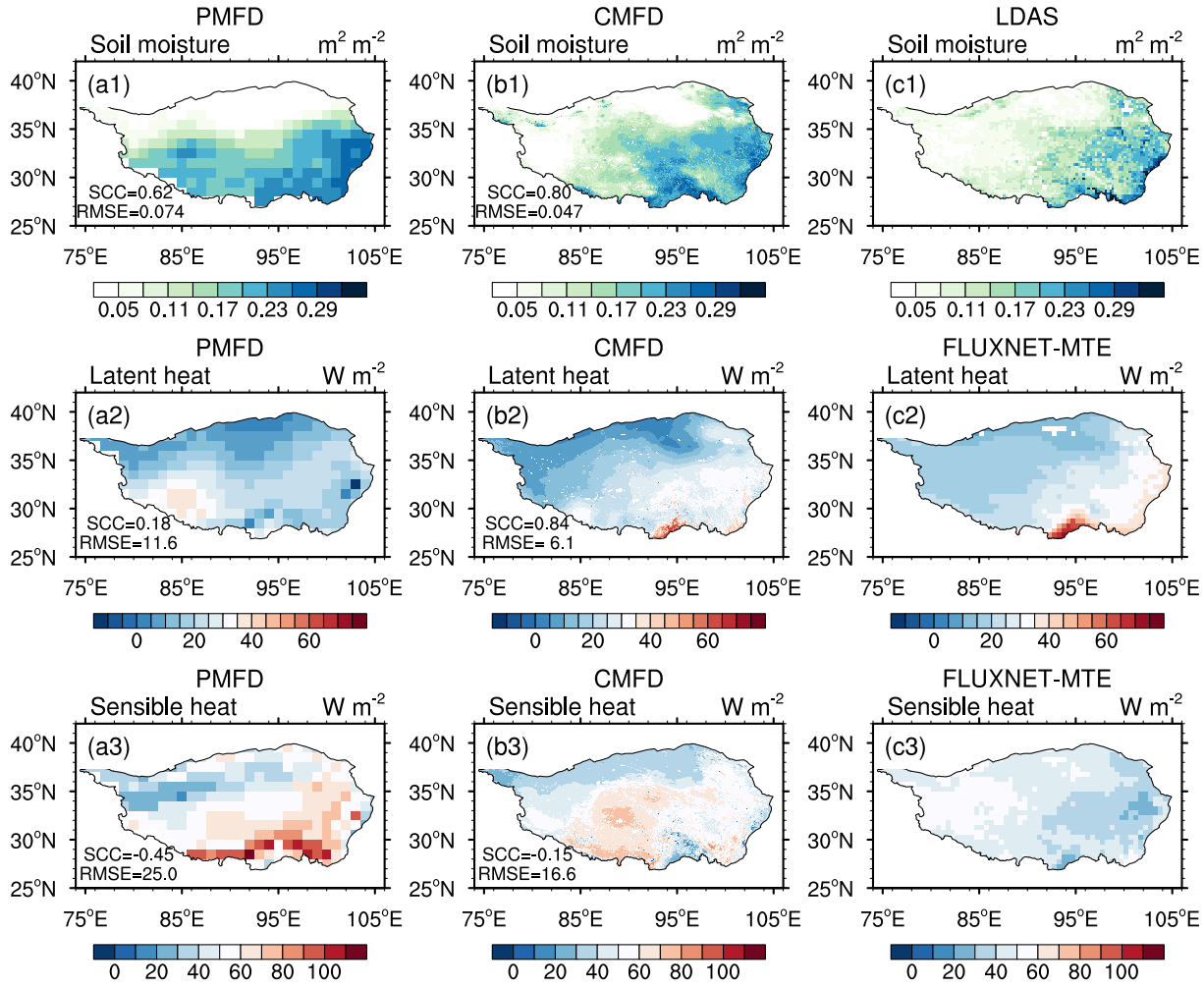

Fig. 13. Spatial patterns of the multi-year averaged annual soil moisture during 2003–07, and the latent and sensible heat flux during 1982–2007; (a1–a3) PMFD, (b1–b3), (c1) CMFD 0.1D, LDAS soil moisture, (c2–c3) FLUXNET-MTE latent and sensible heat flux.

thermal conditions, which is consistent with our results.

Currently, the observations from CMA stations, which are the most important merging datasets for CMFD, are sparse in the northwestern TP and are consequently subject to a large uncertainty of CMFD over this region (Li et al., 2018). With the advancement of observation methods for TP, the Third Tibetan Plateau Atmospheric Scientific Experiment (TIPEX-III) and the Second Tibetan Plateau Scientific Expedition and Research (STEP) constitute an observation system that integrates ground-, air-, and space-based platforms to promote meteorological observations. It is likely that the atmospheric forcing data on TP would be more accurate in the future, further improving simulations of vegetation dynamics on the TP.

5. Conclusions

Vegetation dynamics are vital to water, energy, and carbon exchanges between terrestrial ecosystems and the atmosphere. The quality of simulations of vegetation dynamics simulations in offline land surface models (LSMs) largely depends on the quality and spatial resolution of the meteorological forcing data. In this study, three meteorological forcing datasets were used to drive SSiB4/TRIFFID to explore how accurate and high-spatial-resolution forcing data impact the simulations of vegetation dynamics over the TP. Our main conclusions are as follows.

All three LAI simulations reproduced the spatial distribution and seasonal variability. However, the CMFD 1D run reduces the biases of the spatial distribution of LAI, especially in the western and southwestern regions of the TP. The results show that the LAI simulation in the CMFD 1D decreases the positive biases by 54.5% annually, 54.5% in the spring, 52.1% in the summer, and 71.1% in the autumn, and has a larger SCC and lower RMSE. The Taylor diagram indicated that LAI simulation in the CMFD 0.1D performed best, and the simulation in the PMFD 1D run was the worst. All three simulations reproduced the greening trend on the TP. In addition, the LAI simulation with a higher resolution CMFD (CMFD 0.1D) performed better in terms of spatial distribution.

Regarding the spatial patterns of GPP simulation,

Table Appendix A. List of symbols with units and definition.

Symbol	Units	Definition
A_c	μmol m^{-2} s^{-1}	Net canopy photosynthesis
A_n	μmol m^{-2} s^{-1}	Net leaf photosynthesis
a_{wl}	kgC m^{-2}	Allometric coefficient relating wood to leaf area index
a_{ws}	–	Woody biomass as a multiple of live stem biomass
b_{wl}	–	Allometric exponent relating wood to leaf area index
c_c	Pa	Leaf surface CO_2 partial pressure
c_i	Pa	Leaf internal CO_2 partial pressure
g_s	μmol m^{-2} s^{-1}	Stomatal conductance
h	m	Vegetation height
$\bar{k}$	–	Time-mean value of radiation extinction coefficient
L	m^2 m^{-2}	Actual leaf area index
L_b	m^2 m^{-2}	Balanced leaf area index
N	–	Canopy green leaf fraction
p	–	Leaf phenological state
p_{sf}	Pa	Leaf surface pressure
R_{dc}	μmol m^{-2} s^{-1}	Canopy dark respiration
T	°C	Canopy temperature
T_{off}	°C	Threshold temperature of leaf drop
V	–	Canopy cover fraction
W_c	kgC m^{-2} s^{-1}	Stem carbon density
β	–	Soil moisture availability stress factor
γ_0	–	The minimum value of leaf mortality rate
γ_p	–	Rate of leaf growth
γ_{lm}	–	Leaf mortality rate
ϵ_{dm}	–	Rate of change of leaf mortality rate with soil moisture availability
ϵ_{dt}	–	Rate of change of leaf mortality rate with temperature
θ	m^3 m^{-3}	Soil moisture availability
θ_c	m^3 m^{-3}	Critical soil moisture concentration
θ_{off}	m^3 m^{-3}	Threshold soil moisture availability of leaf drop
θ_w	m^3 m^{-3}	Wilting soil moisture concentration
η_{sl}	kgC m^{-1}	Live stem coefficient
Π	–	Leaf to canopy scaling factor

SSiB4/TRIFFID forced by an upscaled CMFD reduced the positive biases in the southwest, decreased the RMSE, and increased the SCC on the TP. The multi-year averaged-GPP biases in the PMFD 1D run can be largely reduced by adopting more realistic forcing data in the CMFD 1D run. The GPP simulation in CMFD 0.1D further reduced the RMSE and increased the SCC. All the simulations simulated a positive trend, which indicated that carbon fixation on the TP gradually increased.

This study highlights the importance of incorporating more realistic forcing data of higher resolution in simulating LAI and GPP in the LSMs over the complex topography and sparse observations common to the TP.

Acknowledgements. This work was jointly supported by the National Natural Science Foundation of China (Grant Nos. 42130602, 42175136) and the Collaborative Innovation Center for Climate Change, Jiangsu Province, China. The authors thank the Terrestrial Hydrology Research Group, Princeton University, for providing the Global Meteorological Forcing Dataset, which can be found at http://hydrology.princeton.edu/data/pgf/1.0degree/3hourly/. The authors acknowledge the Big Earth Data Platform for Three Poles for providing the China Meteorological Forcing Dataset (1979–2018) and plant functional types map in China.

Electronic supplementary material: Supplementary material is available in the online version of this article at https://doi.org/10.1007/s00376-022-1426-6.

REFERENCES

Alemohammad, S. H., and Coauthors, 2017: Water, Energy, and Carbon with Artificial Neural Networks (WECANN): A statistically-based estimate of global surface turbulent fluxes and gross primary productivity using solar-induced fluorescence. *Biogeosciences*, **14**, 4101–4124, https://doi.org/10.5194/bg-14-4101-2017.

Bastrikov, V., N. MacBean, C. Bacour, D. Santaren, S. Kuppel, and P. Peylin, 2018: Land surface model parameter optimisation using in situ flux data: Comparison of gradient-based

versus random search algorithms (a case study using ORCHIDEE v1.9.5.2). *Geoscientific Model Development*, **11**, 4739–4754, https://doi.org/10.5194/gmd-11-4739-2018.

Chen, A. P., L. Huang, Q. Liu, and S. Piao, 2021: Optimal temperature of vegetation productivity and its linkage with climate and elevation on the Tibetan Plateau. *Global Change Biology*, **27**, 1942–1951, https://doi.org/10.1111/gcb.15542.

Chen, J., 1984: Uncoupled multi-layer model for the transfer of sensible and latent heat flux densities from vegetation. *Bound.-Layer Meteorol.*, **28**, 213–225, https://doi.org/10.1007/bf00121305.

Chen, Y. Y., K. Yang, J. He, J. Qin, J. C. Shi, J. Y. Du, and Q. He, 2011: Improving land surface temperature modeling for dry land of China. *J. Geophys. Res.: Atmos.*, **116**, D20104, https://doi.org/10.1029/2011jd015921.

Collatz, G. J., J. T. Ball, C. Grivet, and J. A. Berry, 1991: Physiological and environmental regulation of stomatal conductance, photosynthesis and transpiration: A model that includes a laminar boundary layer. *Agricultural And Forest Meteorology*, **54**, 107–136, https://doi.org/10.1016/0168-1923(91)90002-8.

Collatz, G. J., L. Bounoua, S. O. Los, D. A. Randall, I. Y. Fung, and P. J. Sellers, 2000: A mechanism for the influence of vegetation on the response of the diurnal temperature range to changing climate. *Geophys. Res. Lett.*, **27**, 3381–3384, https://doi.org/10.1029/1999gl010947.

Cox, P., and C. Jones, 2008: Illuminating the modern dance of climate and CO_2. *Science*, **321**, 1642–1644, https://doi.org/10.1126/science.1158907.

Cox, P. M., C. Huntingford, and R. J. Harding, 1998: A canopy conductance and photosynthesis model for use in a GCM land surface scheme. *J. Hydrol.*, **212–213**, 79–94, https://doi.org/10.1016/s0022-1694(98)00203-0.

Dan, L., X. J. Yang, F. Q. Yang, J. Peng, Y. Y. Li, D. D. Gao, J. J. Ji, and M. Huang, 2020: Integration of nitrogen dynamics into the land surface model AVIM. Part 2: Baseline data and variation of carbon and nitrogen fluxes in China. *Atmospheric and Oceanic Science Letters*, **13**, 518–526, https://doi.org/10.1080/16742834.2020.1819145.

De Kauwe, M. G., and Coauthors, 2015: A test of an optimal stomatal conductance scheme within the CABLE land surface model. *Geoscientific Model Development*, **8**, 431–452, https://doi.org/10.5194/gmd-8-431-2015.

Dong, Z. B., S. Y. Gao, and D. W. Fryrear, 2001: Drag coefficients, roughness length and zero-plane displacement height as disturbed by artificial standing vegetation. *Journal of Arid Environments*, **49**, 485–505, https://doi.org/10.1006/jare.2001.0807.

Duan, Q., and Coauthors, 2006: Model Parameter Estimation Experiment (MOPEX): An overview of science strategy and major results from the second and third workshops. *J. Hydrol.*, **320**, 3–17, https://doi.org/10.1016/j.jhydrol.2005.07.031.

Giambelluca, T. W., D. Hölscher, T. X. Bastos, R. R. Frazão, M. A. Nullet, and A. D. Ziegler, 1997: Observations of albedo and radiation balance over postforest land surfaces in the eastern Amazon Basin. *J. Climate*, **10**, 919–928, https://doi.org/10.1175/1520-0442(1997)010<0919:Ooaarb>2.0.Co;2.

Goudriaan, J., and P. E. Waggoner, 1972: Simulating both aerial microclimate and soil temperature from observations above the foliar canopy. *Netherlands Journal of Agricultural Science*, **20**, 104–124, https://doi.org/10.18174/njas.v20i2.17290.

Guo, D. L., and H. J. Wang, 2013: Simulation of permafrost and seasonally frozen ground conditions on the Tibetan Plateau, 1981-2010,. *J. Geophys. Res.: Atmos.*, **118**, 5216–5230, https://doi.org/10.1002/jgrd.50457.

He, J., K. Yang, W. J. Tang, H. Lu, J. Qin, Y. Y. Chen, and X. Li, 2020: The first high-resolution meteorological forcing dataset for land process studies over China. *Scientific Data*, **7**, 25, https://doi.org/10.1038/s41597-020-0369-y.

Immerzeel, W. W., L. P. H. van Beek, and M. F. P. Bierkens, 2010: Climate change will affect the Asian water towers. *Science*, **328**, 1382–1385, https://doi.org/10.1126/science.1183188.

Jeong, S.-J., C.-H. Ho, H.-J. Gim, and M. E. Brown, 2011: Phenology shifts at start vs. end of growing season in temperate vegetation over the Northern Hemisphere for the period 1982-2008,. *Global Change Biology*, **17**, 2385–2399, https://doi.org/10.1111/j.1365-2486.2011.02397.x.

Jung, M., and Coauthors, 2007: Uncertainties of modeling gross primary productivity over Europe: A systematic study on the effects of using different drivers and terrestrial biosphere models. *Global Biogeochemical Cycles*, **21**, GB4021, https://doi.org/10.1029/2006gb002915.

Jung, M., and Coauthors, 2017: Compensatory water effects link yearly global land CO_2 sink changes to temperature. *Nature*, **541**, 516–520, https://doi.org/10.1038/nature20780.

Lan, X., Y. Li, R. Shao, X. H. Chen, K. R. Lin, L. Y. Cheng, H. K. Gao, and Z. Y. Liu, 2021: Vegetation controls on surface energy partitioning and water budget over China. *J. Hydrol.*, **600**, 125646, https://doi.org/10.1016/j.jhydrol.2020.125646.

Li, C. W., and Coauthors, 2018: The evaluation of SMAP enhanced soil moisture products using high-resolution model simulations and in-situ observations on the Tibetan Plateau. *Remote Sensing*, **10**, 535, https://doi.org/10.3390/rs10040535.

Li, H. Q., W. D. Guo, G. D. Sun, Y. C. Zhang, and C. B. Fu, 2011: A new approach for parameter optimization in land surface model. *Adv. Atmos. Sci.*, **28**, 1056–1066, https://doi.org/10.1007/s00376-010-0050-z.

Liang, J. J., Z.-L. Yang, X. T. Cai, P. R. Lin, H. Zheng, and Q. Y. Bian, 2020: Modeling the impacts of nitrogen dynamics on regional terrestrial carbon and water cycles over China with Noah-MP-CN. *Adv. Atmos. Sci.*, **37**, 679–695, https://doi.org/10.1007/s00376-020-9231-6.

Liu, J. G., C. X. Shi, S. Sun, J. J. Liang, and Z.-L. Yang, 2019a: Improving land surface hydrological simulations in China using CLDAS meteorological forcing data. *J. Meteor. Res.*, **33**, 1194–1206, https://doi.org/10.1007/s13351-019-9067-0.

Liu, L. B., Y. Wang, Z. Wang, D. L. Li, Y. T. Zhang, D. H. Qin, and S. C. Li, 2019b: Elevation-dependent decline in vegetation greening rate driven by increasing dryness based on three satellite NDVI datasets on the Tibetan Plateau. *Ecological Indicators*, **107**, 105569, https://doi.org/10.1016/j.ecolind.2019.105569.

Long, B., B. Q. Zhang, C. S. He, R. Shao, and W. Tian, 2018: Is there a change from a warm-dry to a warm-wet climate in the Inland River area of China? Interpretation and analysis through surface water balance *J. Geophys. Res.: Atmos.*, **123**, 7114–7131, https://doi.org/10.1029/2018jd028436.

Lü, J. H., and J. J. Ji, 2002a: A simulation study of atmosphere-vegetation interactions over the Tibetan Plateau. Part Ⅰ: Physical fluxes and parameters. *Chinese Journal of Atmospheric*

Sciences, **26**, 111–126, https://doi.org/10.3878/j.issn.1006-9895.2002.01.11. (in Chinese with English abstract)

Lü, J. H., and J. J. Ji, 2002b: A simulation study of atmosphere-vegetation interaction over the Tibetan Plateau. Part Ⅱ: Net primary productivity and leaf area index. *Chinese Journal of Atmospheric Sciences*, **26**(2), 255–262, https://doi.org/10.3878/j.issn.1006-9895.2002.02.11. (in Chinese with English abstract)

Meng, X., and Coauthors, 2018: Simulated cold bias being improved by using MODIS time-varying albedo in the Tibetan Plateau in WRF model. *Environmental Research Letters*, **13**, 044028, https://doi.org/10.1088/1748-9326/aab44a.

Ran, Y. H., X. Li, L. Lu, and Z. Y. Li, 2012: Large-scale land cover mapping with the integration of multi-source information based on the Dempster–Shafer theory. *International Journal of Geographical Information Science*, **26**, 169–191, https://doi.org/10.1080/13658816.2011.577745.

Ren, Y. H., K. Yang, H. Wang, L. Zhao, Y. Y. Chen, X. Zhou, and Z. La, 2021: The South Asia monsoon break promotes grass growth on the Tibetan Plateau. *J. Geophys. Res.: Biogeosci.*, **126**, e2020JG005951, https://doi.org/10.1029/2020jg005951.

Sellers, P. J., Y. Mintz, Y. C. Sud, and A. Dalcher, 1986: A simple biosphere model (SIB) for use within general circulation models. *J. Atmos. Sci.*, **43**, 505–531, https://doi.org/10.1175/1520-0469(1986)043<0505:Asbmfu>2.0.Co;2.

Sellers, P. J., and Coauthors, 1996: A revised land surface parameterization (SiB2) for atmospheric GCMS. Part I: Model formulation. *J. Climate*, **9**, 676–705, https://doi.org/10.1175/1520-0442(1996)009<0676:Arlspf>2.0.Co;2.

Sheffield, J., G. Goteti, and E. F. Wood, 2006: Development of a 50-year high-resolution global dataset of meteorological forcings for land surface modeling. *J. Climate*, **19**, 3088–3111, https://doi.org/10.1175/jcli3790.1.

Shen, M. G., and Coauthors, 2015: Evaporative cooling over the Tibetan Plateau induced by vegetation growth. *Proceedings of the National Academy of Sciences of the United States of America*, **112**, 9299–9304, https://doi.org/10.1073/pnas.1504418112.

Su, F. G., X. L. Duan, D. L. Chen, Z. C. Hao, and L. Cuo, 2013: Evaluation of the global climate models in the CMIP5 over the Tibetan Plateau. *J. Climate*, **26**, 3187–3208, https://doi.org/10.1175/jcli-d-12-00321.1.

Sun, S. B., and Coauthors, 2016: Improving soil organic carbon parameterization of land surface model for cold regions in the Northeastern Tibetan Plateau, China. *Ecological Modelling*, **330**, 1–15, https://doi.org/10.1016/j.ecolmodel.2016.03.014.

Wu, G. X., and Coauthors, 2007: The influence of mechanical and thermal forcing by the Tibetan Plateau on Asian climate. *Journal of Hydrometeorology*, **8**, 770–789, https://doi.org/10.1175/jhm609.1.

Xiao, Z. Q., S. L. Liang, J. D. Wang, P. Chen, X. J. Yin, L. Q. Zhang, and J. L. Song, 2014: Use of general regression neural networks for generating the GLASS leaf area index product from time-series MODIS surface reflectance. *IEEE Trans. Geosci. Remote Sens.*, **52**, 209–223, https://doi.org/10.1109/tgrs.2013.2237780.

Xue, Y., P. J. Sellers, J. L. Kinter, and J. Shukla, 1991: A simplified biosphere model for global climate studies. *J. Climate*, **4**, 345–364, https://doi.org/10.1175/1520-0442(1991)004<0345:Asbmfg>2.0.Co;2.

Yang, K., J. He, W. J. Tang, J. Qin, and C. C. K. Cheng, 2010: On downward shortwave and longwave radiations over high altitude regions: Observation and modeling in the Tibetan Plateau. *Agricultural and Forest Meteorology*, **150**, 38–46, https://doi.org/10.1016/j.agrformet.2009.08.004.

Yang, K., Y. Y. Chen, J. He, L. Zhao, H. Lu, J. Qin, D. H. Zheng, and X. Li, 2020: Development of a daily soil moisture product for the period of 2002–2011 in Chinese mainland. *Science China Earth Sciences*, **63**, 1113–1125, https://doi.org/10.1007/s11430-019-9588-5.

Yang, X. J., L. Dan, F. Q. Yang, J. Peng, Y. Y. Li, D. D. Gao, J. J. Ji, and M. Huang, 2019: The integration of nitrogen dynamics into a land surface model. Part 1: Model description and site-scale validation. *Atmospheric and Oceanic Science Letters*, **12**, 50–57, https://doi.org/10.1080/16742834.2019.1548246.

Yu, M., H. S. Chen, and Z. B. Sun, 2011: Seasonal and interannual variations of boreal vegetation simulated by an improved interactive canopy model (ICM). *Chinese Journal of Atmospheric Sciences*, **35**, 571–588, https://doi.org/10.3878/j.issn.1006-9895.2011.03.16. (in Chinese with English abstract)

Zhan, X. W., Y. K. Xue, and G. J. Collatz, 2003: An analytical approach for estimating CO_2 and heat fluxes over the Amazonian region. *Ecological Modelling*, **162**, 97–117, https://doi.org/10.1016/s0304-3800(02)00405-2.

Zhang, T., and Coauthors, 2018: Water availability is more important than temperature in driving the carbon fluxes of an alpine meadow on the Tibetan Plateau. *Agricultural and Forest Meteorology*, **256–257**, 22–31, https://doi.org/10.1016/j.agrformet.2018.02.027.

Zhang, Y. Q., and Coauthors, 2016: Multi-decadal trends in global terrestrial evapotranspiration and its components. *Scientific Reports*, **6**, 19124, https://doi.org/10.1038/srep19124.

Zhang, Z. Q., Y. K. Xue, G. MacDonald, P. M. Cox, and G. J. Collatz, 2015: Investigation of North American vegetation variability under recent climate: A study using the SSiB4/TRIFFID biophysical/dynamic vegetation model. *J. Geophys. Res.: Atmos.*, **120**, 1300–1321, https://doi.org/10.1002/2014jd021963.

Zhao, W., and A. N. Li, 2015: A review on land surface processes modelling over complex terrain. *Advances in Meteorology*, **2015**, 607181, https://doi.org/10.1155/2015/607181.

Zhong, L., Y. M. Ma, Y. K. Xue, and S. Piao, 2019: Climate change trends and impacts on vegetation greening over the Tibetan Plateau. *J. Geophys. Res.: Atmos.*, **124**, 7540–7552, https://doi.org/10.1029/2019jd030481.

Zhu, Z. C., and Coauthors, 2016: Greening of the Earth and its drivers. *Nature Climate Change*, **6**, 791–795, https://doi.org/10.1038/nclimate3004.